J. Fluid Mech. (2007), *vol.* 588, *pp.* 131–152. © 2007 Cambridge University Press
doi:10.1017/S0022112007007483 Printed in the United Kingdom

Surface breakup and air bubble formation by drop impact in the irregular entrainment region

Y. TOMITA, T. SAITO AND S. GANBARA

Faculty of Education, Hokkaido University of Education, 1-2 Hachiman-cho, Hakodate, Hokkaido 040-8567, Japan
tomita@cc.hokkyodai.ac.jp

(Received 7 September 2006 and in revised form 12 May 2007)

Drop impact on a water surface can be followed by underwater sounds originating not at the drop impact but when the entrained bubbles oscillate. Although the sound mechanism in the regular bubble entrainment region is well-known, there is less knowledge on the impact phenomena in the irregular bubble entrainment region where various situations can exist, such as many types of bubble formation or even no bubble generation under some conditions. In the present study, the aim is to clarify the dynamics of the water surface after the impact of a primary drop, mainly with diameter 5.2, 5.7 and 6.2 mm, each of which is accompanied by a single satellite drop. Special attention was paid to the breakup behaviour of the water surface for Froude number $Fr < 300$. It was found that three underwater sounds were generated for a single drop impact, besides the sound due to impact itself. The first two were audible to the human ear, but the third one was almost inaudible. The first underwater sound resulted from the oscillation of a single air bubble formed as a result of the satellite drop impact on the bottom of the contracting cavity, and the second sound was due to the oscillation of air bubbles generated during the collapse of the water column. The formation of these air bubbles strongly depends on the Froude number, Weber number (or Bond number) and the aspect ratio of the drop at impact, although involving probability characteristics. Furthermore it is suggested that an air bubble entrapped in a water column plays an important role in increasing the probability of contact between the column surface and the curved free surface. A Japanese Suikinkutsu was introduced as an application of drop-impact-induced sounds. Using an open-type Suikinkutsu an additional experiment was carried out with larger drops with average diameters of 6.2, 7.2 and 7.8 mm.

1. Introduction

Air bubbles can be entrapped by the impact of a drop falling on a water surface, subsequently producing underwater sounds. In our daily life we hear a familiar sound of dripping water like 'Po—cha-nn', which is an onomatopoeic sound expressed in Japanese. In the natural environment we often hear noises from rain drops which have power spectra peaks at around 14 kHz (Scrimger 1985; Nystuen 1986) and these peak values are reduced in the presence of wind at sea (Medwin, Kurgan & Nystuen 1990). Important parameters associated with the bubble formation and induced underwater sounds are considered to be the drop diameter d_D and drop impact velocity V_{imp}, which make a parameter plane containing two audible regions. One is called the regular bubble entrainment region where relatively small air bubbles are always formed owing

to pinch-off phenomena, appearing at the bottom of a conical-shaped free surface (Prosperetti, Crum & Pumphrey 1989; Pumphrey & Elmore 1990; Oguz & Prosperetti 1990). The other is the irregular bubble entrainment region where a variety of bubble formations can take place, and in which there are still issues remaining to be solved. It is known that bubble formation is significantly affected by surface tension. This is easily confirmed by adding surfactant to water, resulting in a decrease in surface tension. As a result the number of air bubbles decreases, leading to a reduction in noise level (Prosperetti *et al.* 1989).

The regular entrainment region is very accurately known and bounded by two limiting curves with $We \propto Fr^{1/4}$ for the upper limit and $We \propto Fr^{1/5}$ for the lower limit (Oguz & Prosperetti 1990), where Fr is the Froude number defined as $Fr = V_{imp}^2/(gd_D)$, and We the Weber number defined as $We = \rho d_D V_{imp}^2/\sigma$ with g being the acceleration due to gravity, ρ and σ the density and surface tension of water, respectively. Pumphrey & Elmore (1990) named the irregular bubble entrainment region the Franz irregular entrainment region (Franz 1959) and found that the splash was so energetic that bubbles were nearly always entrained. In this region, however, various patterns of bubble formation could exist and under some conditions no bubble sounds occur. On account of this characteristic of bubble formation, the irregular entrainment region is generally believed to involve a probability. In this region drop impact often also produces a number of minute bubbles when a water column collapses.

Oguz & Prosperetti (1989) suggested a mechanism of bubble cloud formation. During the process after drop impact, the gap between the water column surface and curved free surface becomes small, eventually inducing unstable waves on the both surfaces due to Taylor instability. Since the water column continues downward, two crests of the fluctuating surfaces could come into contact. Consequently film rupture occurs, resulting in the formation of a toroidal bubble which is unstable, and finally breaks up into numerous minute air bubbles. More recently Thoroddsen, Etoh & Takehara (2003) succeeded in capturing similar phenomena generated soon after the drop impact by means of high-speed video photography. In the irregular bubble entrainment region, if the initial drop height is less than a couple of metres, the impact velocity is estimated to be much smaller than the terminal velocity. In contrast to raindrops, in daily life drops are often created as a result of detachment from a material surface. Thus the drop size depends on the condition of contact with the surface. After the separation of the water bridge developed at the rear side of a drop (Peregrine, Shoker & Symon 1990; Zhang & Basaran 1995), a primary drop freely falls downward onto a free surface. For a drop with size larger than a critical one, a satellite drop is always produced due to the competition between gravity and surface tension effects. In the irregular entrainment region, however, there are still unsolved problems associated with the mechanism of surface breakup and bubble formation, which are closely related to underwater sound generation.

In Japan, we have the 'Suikinkutsu', a water harp jar, which is a traditional musical instrument often set up at Japanese gardens and dating back to the Edo period (Tatsui 2000). Drop impact phenomena occur inside a water jar which is placed upside-down under the ground near a water basin. Figure 1 shows a schematic drawing of a traditional Suikinkutsu (Tatsui 2000; Tomita 2004). It is said that a Suikinkutsu is an acoustic device using sounds generated by draining water overflowing from a water basin where people wash their hands when entering a tea-ceremony room. A Suikinkutsu usually has a hole in the bottom of the water jar, called a 'Suimon', and its optimum diameter is considered to be 20–30 mm. Water draining through this hole falls on the water surface. Combinations of drops and water mass can produce

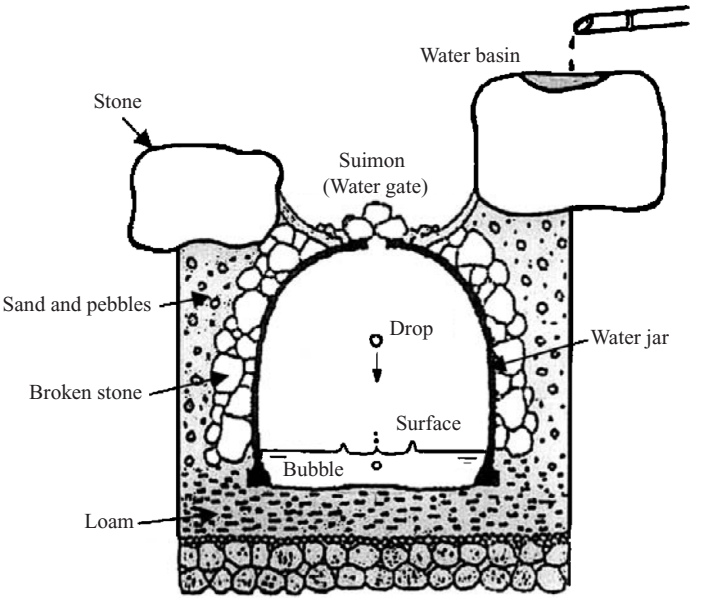

FIGURE 1. An illustration of a traditional Japanese Suikinkutsu.

a variety of underwater sounds, from single drop impact and those resulting from running water. A typical water jar for Suikinkutsu has a maximum inner diameter of about 500 mm and a height of 400–600 mm, but some are more than 1 m in height. At the base of a Suikinkutsu, water is supplied up to a certain constant level controlled by overflowing. The jar is covered with various sized broken stones which make a space in which the original bubble sounds grow, yielding an effective resonant sound. The sound emitting from a Suikinkutsu is very clear and relaxing.

Watanabe (2004) analysed the acoustic mechanism of a portable Suikinkutsu, a 'Hana Suikinkutsu', by employing water drops with an average diameter of 7.5 mm. He captured impact phenomena with a high-speed camera and simultaneously measured the original and reverberant sounds. He found that three criteria are essentially important for the Suikinkutsu sound: (i) a sufficiently large bubble, (ii) a drop period longer than 2.0 s and (iii) a drop distance in the range of 300–400 mm. A good tonal quality of sound was obtained under these conditions when the drop distance was 365 mm and the drop period longer than 2.0 s, creating the original sound of a Hana Suikinkutsu with the frequency of 850 Hz. This is equivalent to the sound resulting from the oscillation of a spherical bubble with equivalent diameter of 7.5–8.0 mm. Although a larger drop impacting on the water surface generated a better sound (Watanabe 2004), each individual has their own preference.

In the present study, we intend to elucidate the mechanism of air bubble formation in the irregular bubble entrainment region by employing mainly three drop diameters: 5.2, 5.7 and 6.2 mm, all of which are followed by single satellite drops. Special attention will be given to the water surface breakup near the bottom of a falling water column since it is closely connected with the second bubble formation. Furthermore, an open-type Suikinkutsu is examined by taking additional drops of the average diameters of 7.2 and 7.8 mm, which is a similar experiment to that of Watanabe (2004).

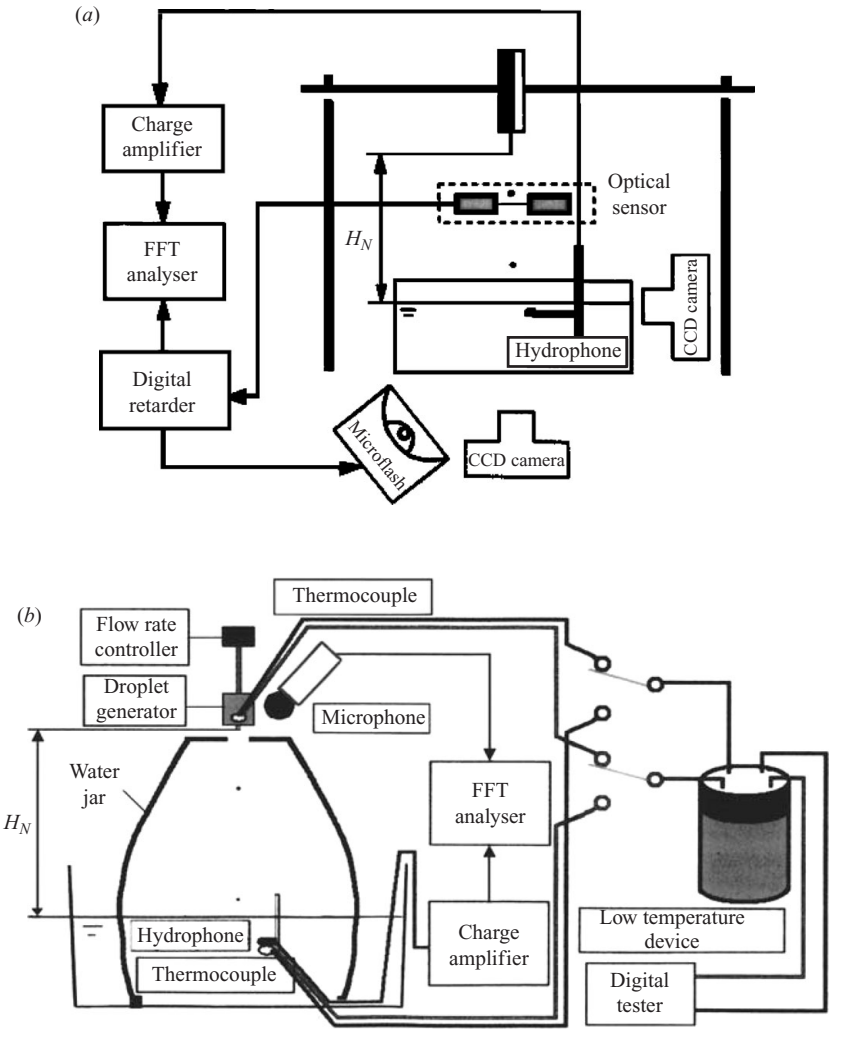

FIGURE 2. Experimental set-ups of (*a*) a water tank and (*b*) an open-type Suikinkutsu.

2. Experimental apparatus and methods

Figure 2(*a*) shows a diagram of the experimental setup primarily used in the present study and 2(*b*) is a schematic view of the sound measurement for an open-type Suikinkutsu. In figure 2(*a*) water drops are generated by employing a nozzle filled with highly hygroscopic material that freely impacted on a water surface, whereas for figure 2(*b*) a double-piled wire netting was used for larger drop generation. During the dropping period a water drop changes from being prolate to oblate several times due to gravity and surface tension forces. Finally it collides with the free surface in the form of a spheroid, not a spherical shape. An equivalent drop diameter d_D is, therefore, determined as the diameter of a sphere having the same volume as the spheroid using the relation $d_D = (a\,b^2)^{1/3}$, where b is the horizontal drop diameter and a is the vertical drop diameter at impact. As shown in figure 2(*a*) the main experiment was carried out using an open-type rectangular water tank with the dimensions of $400 \times 300 \times 200$ mm at atmospheric pressure and room temperature (15 °C). The drop

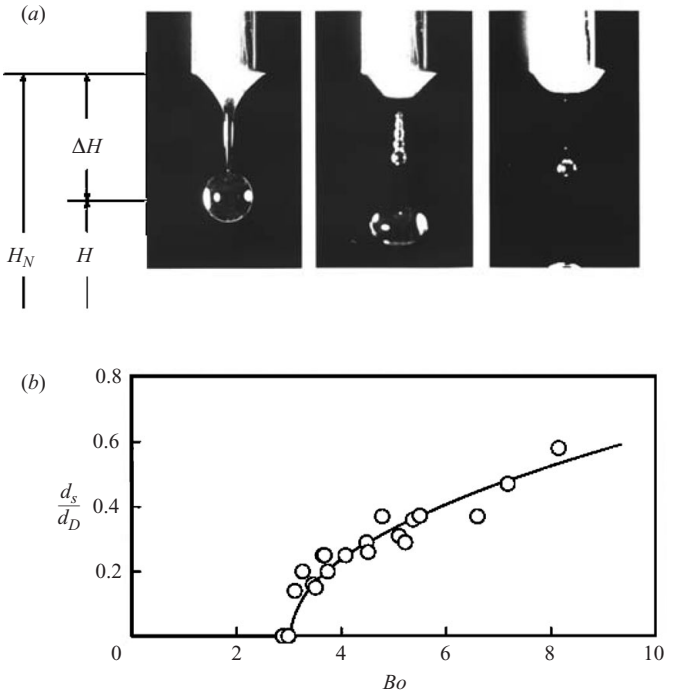

FIGURE 3. Primary and satellite drop formations: (*a*) three selected snapshots of the formation of a 6.2 mm sized primary drop, followed by a satellite drop; (*b*) satellite drop diameter divided by primary drop diameter as a function of the Bond number.

diameters employed here were mainly 5.2, 5.7 and 6.2 mm and the dripping height H_N, i.e. the distance from the nozzle exit to the quiescent free surface, was widely varied. The drop impact velocity V_{imp} was directly measured from the optical images taken with high-speed video photography. The impact velocity was also evaluated by using the initial drop height, $H\,(=H_N-\Delta H)$, defined as the distance between the centre of the primary drop falling freely and the water surface, where ΔH is the dripping length as indicated in figure 3(*a*), depending on the primary drop diameter. While falling a drop cut off light from a diode to create a trigger signal for starting a measuring system. Underwater sounds were detected with a hydrophone (B & K 8103) located 50 mm from the impact point and 50 mm below the free surface and amplified with a charge amplifier (B & K 2635); then the signals were fed into a FFT analyser (Ono Sokki CF-3200J). Figure 3 shows (*a*) three selected snapshots of the formation of a 6.2 mm-sized drop and (*b*) the ratio of the satellite and primary drop diameters, i.e. d_s/d_D, versus Bond number defined as $Bo(=We/Fr)=(\rho g/\sigma)d_D^2$. As mentioned above, we used drops with the average diameters of mainly 5.2, 5.7 and 6.2 mm, which were measured with the maximum error less than 5 %. Although the three Bond numbers, 3.62, 4.35 and 5.15, are fixed corresponding to these average drop diameters, drop with different sizes, ranging from 4.64 to 7.80 mm, are also included in figure 3(*b*) to give a more detailed relation between d_s/d_D and Bo. The solid line in figure 3(*b*) is a best fit curve for the experimental data, determined using the method of least squares. It is expressed by

$$d_s/d_D = 0.24\sqrt{Bo-3.0}. \tag{1}$$

No satellite drop formation occurred for $Bo<3.0$, which corresponded to $d_D<4.7$ mm. The whole motion of the surface dynamics was photographed with

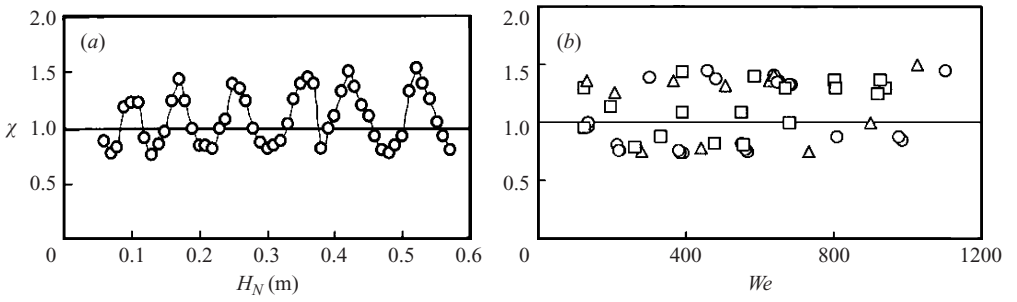

FIGURE 4. Aspect ratio χ of a drop at impact as a function of (*a*) the dripping height H_N for a drop diameter of 6.2 mm and (*b*) the Weber number *We* for three drop diameters denoted as follows: ○, 6.2 mm; △, 5.7 mm; □, 5.2 mm.

a high-speed digital video camera (SANPICO Photron Fastcam) with rate of 4500 frames s^{-1}. Furthermore we obtained snapshots of the phenomena simultaneously taken from two different directions at right angles, viewing both the air and water layers, and the resultant images were recorded on the focal planes of two CCD cameras (Nikon Coolpix IV). They were illuminated by two Xenon flashes each with pulse duration of 2 μs, employing diffused sheets for obtaining transparent images.

As pointed out in Chapman & Critchlow (1967) and Tomita, Kasai & Miura (2003), a drop changes its shape periodically during the falling process depending on the initial drop height as well as the drop diameter. Accordingly the dynamics of the free surface is influenced by the drop shape at the impact as well. Figure 4 shows the aspect ratio χ of a drop at impact, showing (*a*) a specific example of the aspect ratio vs. dripping height curve for $d_D = 6.2$ mm and (*b*) the aspect ratio χ as a function of the Weber number for three average drop diameters of 5.2, 5.7 and 6.2 mm, where χ is the ratio of the horizontal drop diameter, *b*, divided by the vertical drop diameter, *a*. If $\chi > 1$ the drop shape is oblate, whereas if $\chi < 1$ it is prolate, upon contact with the water surface. When a primary drop was created immediately after the separation from the water bridge, the initial drop shape tended to be prolate as clearly seen in figure 3(*a*). During the falling period, it changes shape alternately from prolate to oblate but mostly appears in the form of an oblate spheroid.

For example, if we take the conditions of $d_D = 6.2$ mm, where $\Delta H = 16$ mm, and $H_N = 420$ mm, we obtain the period of the oscillation of a drop to be 44.9 ms by applying $T = 2\pi/\omega$, where ω is the angular frequency formulated as $\omega^2 = n(n-1)(n+2)\sigma/(\rho R^3)$ with n being the order of the oscillation mode, σ the surface tension, ρ the density of water and R the radius of a drop (Rayleigh 1894). The time required to impact can be calculated as 287 ms by neglecting air drag, so the drop could oscillate 6.4 times during the falling period, slightly large compared to the result observed from figure 4(*a*) where the drop oscillaties nearly six times during the dripping height $H_N = 420$ mm. Accordingly, when assembling the data for various average diameters, as shown in figure 4(*b*), the aspect ratios were slightly different because an individual average drop diameter involved unavoidable error, presumably resulting from the reproducibility of the dripping length ΔH. The aspect ratio χ ranges from 0.7 to 1.5. When a prolate drop impacted on a water surface, the resultant splash was weak compared to the oblate drop case. This suggests that the drop aspect ratio may affect surface breakup. This will be discussed later.

Most of the data used in this paper were obtained from high-speed video images. In addition high-quality snapshots using the Xenon flashes as light sources were taken. An experiment was also performed by using drops with the average diameters of 6.2,

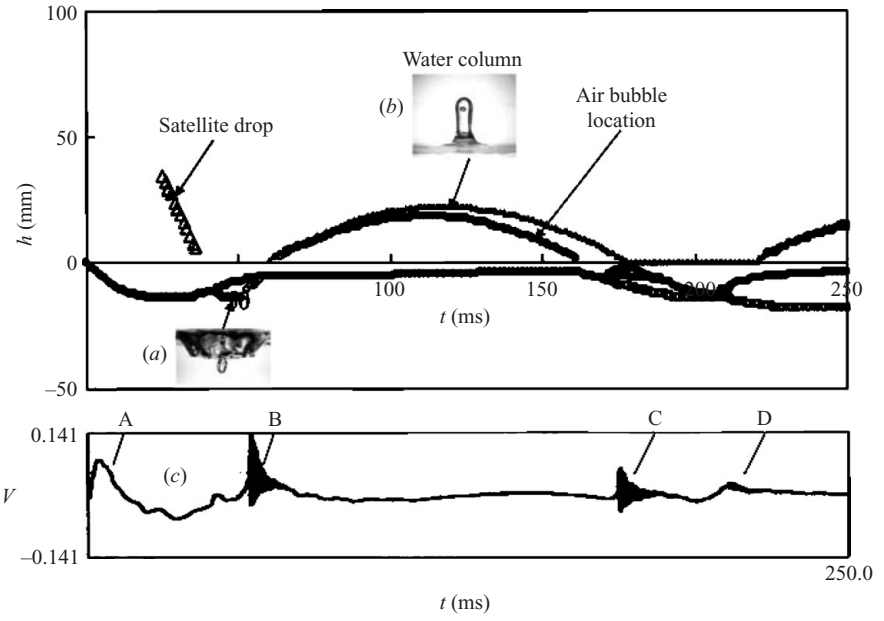

FIGURE 5. Overall motion of the free surface together with other variables for the conditions of $d_D = 6.2$ mm and $V_{imp} = 2.81\,\mathrm{m\,s^{-1}}$ ($Fr = 130$, $We = 663$). (*a*) A projection due to satellite drop impact and (*b*) a water column containing an air bubble. (*c*) An example of underwater sound records corresponding to the free-surface digram above.

7.2 and 7.8 mm in order to investigate the sound of an open-type Suikinkutsu, whose inner maximum diameter was 430 mm and its height was 590 mm as illustrated in figure 2(*b*). Suikinkutsu sounds were detected with a microphone (JEIC TYPE1015A) placed outside the water jar. This measuring system enables us to explore the effects of both water flow rate and water temperature on the Suikinkutsu sound.

3. Results and discussion

Figure 5 shows an example of the time evolution of the free-surface dynamics along the symmetry axis after drop impact for the conditions of $d_D = 6.2$ mm and $V_{imp} = 2.81\,\mathrm{m\,s^{-1}}$, which gave Froude and Weber numbers of 130 and 663, respectively. The time t is defined as the elapsed time measured from the instant of the drop impact on the free surface. In this figure (*a*) indicates a projection due to satellite drop impact and (*b*) is a water column developed from a splash jet, which contains an air bubble. A typical record of underwater sounds is shown in figure 5(*c*). Four acoustic pressure peaks appear at different times. The first, denoted by A, is due to the drop impact on the free surface and followed by three others termed B, C and D. As demonstrated by Obara, Bourne & Field (1995) and Bourne, Obara & Field (1996) the peak A must be caused by the water hammer pressure, generally having a very short pulse duration. However here it seems relatively longer. This is because the hydrophone employed here performs less well for such a rapid increase in pressure. On the other hand, it is seen that the signals B, C and D consist of damped sinusoidal waves.

3.1. *Early surface dynamics and the first bubble formation*

Figure 6 shows five pairs of snapshots simultaneously taken in both the air (above) and water (below) layers, indicating an early stage of the free-surface dynamics

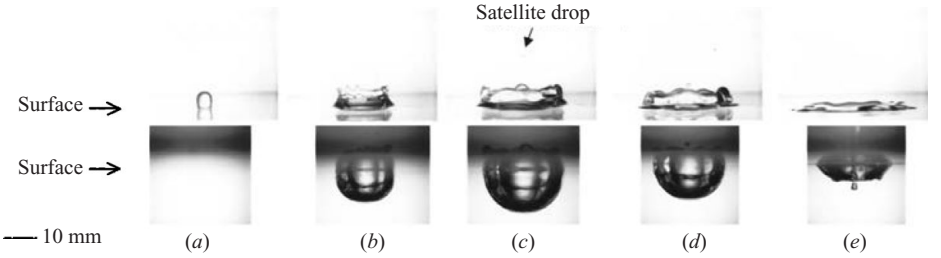

FIGURE 6. Simultaneous records of the early dynamics of a free surface after drop impact taken in air (above) and in water (below) for the same conditions as figure 5. Time t is measured from the instant of drop impact on the free surface. t (ms): (*a*) 0, (*b*) 5, (*c*) 25, (*d*) 30, (*e*) 51.

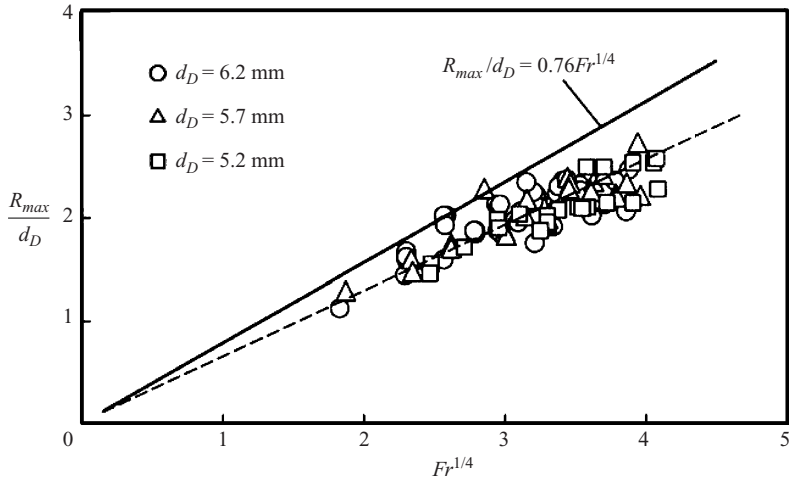

FIGURE 7. Maximum cavity depth R_{max}/d_D versus $Fr^{1/4}$. The solid line is a theoretical prediction of R_{max}/d_D determined by assuming no energy dissipation during the cavity motion and the dashed line is a best-fit curve for the experimental data obtained by the method of least squares.

for the same conditions as figure 5. Immediately after the impact, a thin liquid film was elevated to form a splash, and then developed into a crown (Worthington 1908). The impacted free surface was deformed, forming a hemispherical cavity which finally reached a maximum size, R_{max}, which is measured from the initial quiescent water surface. When the maximum depth is attained, the water surface is in the fully stretched state. According to the procedure associated with the energetic considerations of drop impact carried out by Pumphrey & Elmore (1990) and Liow (2001), we obtain the maximum cavity depth as

$$R_{max}/d_D = 0.76Fr^{1/4}. \tag{2}$$

The crown began to collapse when small droplets were detached from the rim of individual liquid ligaments; subsequently capillary waves were generated and travelled towards the centre of the cavity bottom. Underneath the cavity an outward water flow stopped, and then started to move upward to produce a water jet. Experimental data for the maximum cavity depth, R_{max}/d_D, are plotted against $Fr^{1/4}$ in figure 7 for three drop diameters, i.e. $d_D = 5.2$, 5.7 and 6.2 mm, in which the solid line is

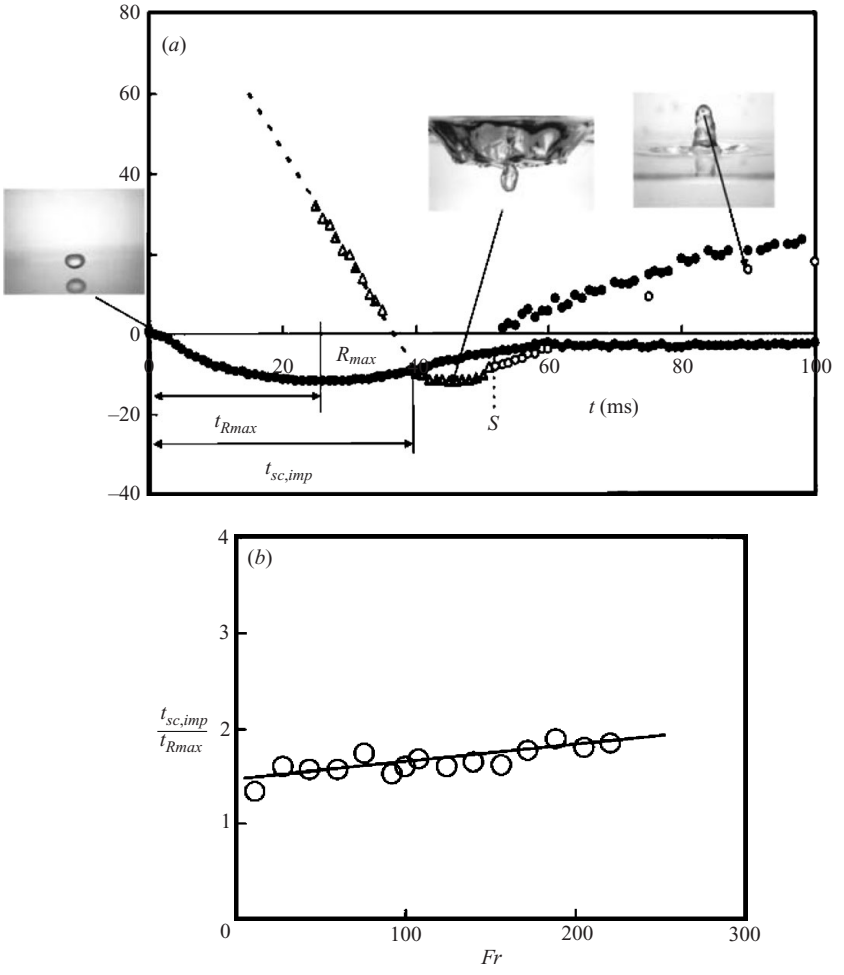

FIGURE 8. Impact of a satellite drop on a curved free surface: (*a*) early surface dynamics and the definition of variables with *S* being the point of bubble formation, (*b*) impact time, $t_{sc,imp}$, divided by the time at maximum cavity depth, t_{Rmax}, as a function of Froude number, *Fr* for $d_D = 6.2$ mm.

the theoretical prediction given by (2). The dashed line is a best fit curve for the experimental data given by the method of least squares. We can evaluate the slope of the $Fr^{1/4}$ dependence to be 0.64 which is 84 % of the theoretical one. The difference between the theory and experiment is because the theory is derived by assuming a perfect energy transfer: the potential energy of a drop completely changes into kinetic energy at impact, then converts into the work done to create a cavity. However, in a real situation, there is energy dissipation due to such factors as air drag around a falling drop and splash formation after the drop impact. Furthermore the water flow around a cavity does not stop instantaneously when it reaches a maximum size.

For a drop with an initial height less than 1 m, a satellite drop tended to impact on the cavity bottom before creating a water jet which would develop into a water column. Figure 8 shows the early stage of surface dynamics for the case of $d_D = 6.2$ mm and $Fr = 130$ where a satellite drop impacted on the contracting free surface. In (*a*) the variables employed here are defined, with *S* being the instant of air bubble formation

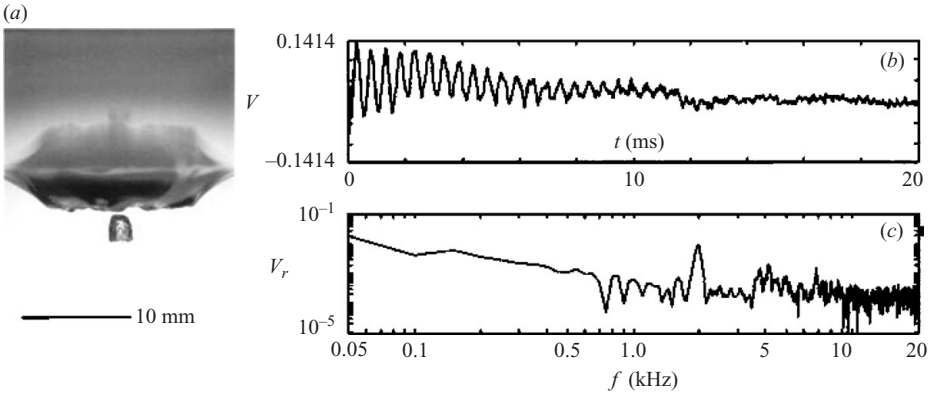

FIGURE 9. First bubble sound generated after the air bubble formation due to satellite drop impact on the contracting cavity surface in the case of $Fr = 108$ and $We = 555$ ($d_D = 6.2$ mm). (a) A snapshot of an isolated air bubble taken at $t = 55$ ms; (b) and (c) the resultant underwater sound signal and its power spectrum, respectively.

and (b) shows the satellite impact time, $t_{sc,imp}$, divided by the time at the maximum cavity depth, t_{Rmax}, as a function of Froude number, Fr. Obviously the impact time linearly increases as Fr increases. Like a primary drop, satellite drop impact can produce a small depression at the bottom of a cavity as demonstrated in figures 5(a) and 6(e). When the kinetic energy at primary drop impact is small, the subsequent energy of the satellite drop impact may be small as well. Consequently, the free surface does not separate, resulting in the deformation of the cavity elongating behind the satellite. On the other hand, for a higher Fr, a canopy, a very large bubble, could be formed as a result of joining of splash sheets over the top of a crown from all sides (Liow 2001). In this case no underwater sounds were generated. On the other hand, for an intermediate Froude number, $50 < Fr < 150$, an air bubble was entrapped with almost 100 % probability as typically indicated in figure 9 where (a) is a snapshot taken immediately after the bubble formation for the case where $d_D = 6.2$ mm and $Fr = 108$ and $We = 555$, and (b) and (c) are the resultant underwater acoustic signal and its power spectrum, respectively. The prominent frequency of 2 kHz is believed to come from the oscillation of an air bubble with 1.6 mm in radius as measured from figure 9(a). Although the air bubble is usually non-spherical, the induced sound is predominantly due to its volume pulsation (Strasberg 1956). The frequency of the volume pulsation of a bubble can be expressed as

$$f_B = \frac{1}{2\pi R_e}\sqrt{\frac{3\gamma p_\infty}{\rho}}, \tag{3}$$

where R_e is the equivalent bubble radius, p_∞ the atmospheric pressure and γ the ratio of specific heats of air (Minnaert 1933). This sound is called the first bubble sound, i.e. the first underwater sound due to air bubble oscillation. Transient acoustic peaks designated by B in figure 5 and in figure 9(b) are both attributed to the oscillation of an isolated air bubble captured in the so-called 'Pumphrey' fashion (Pumphrey & Elmore 1990). When we removed the satellite drop, no first bubble sound resulted (Tomita *et al.* 2003). The frequencies of the first bubble sound both in the regular bubble entrainment region and in the irregular bubble entrainment region are shown in figure 10 for various bubble radii. The experimental data of frequencies measured

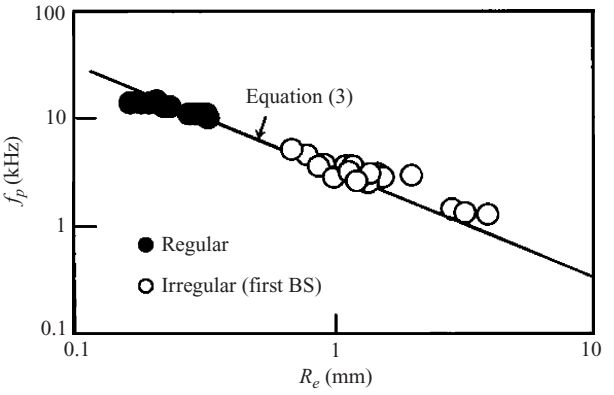

FIGURE 10. Frequency at a power peak f_p versus equivalent bubble radius R_e, where the solid line denotes the theoretical prediction derived from equation (3).

as a prominent power peak, f_p, are in good agreement with the theory, (3), denoted by a solid line. As observed in figure 9(*a*) the first bubble formation in the irregular entrainment region is quite different from that in the regular entrainment region where a bubble is produced by pinch-off phenomena (Prosperetti *et al.* 1989; Pumphrey & Elmore 1990; Oguz & Prosperetti 1990).

It may be helpful to compare to micro-jet impact during cavitation bubble collapse (Tomita & Shima 1990; Blake, Tomita & Tong 1998) to the drop impact, although there are some differences between the two phenomena. For instance, the velocity of a liquid jet formed during cavitation bubble collapse is more than 30 times larger than the drop impact case and their shapes are different since a water drop is spheroid whereas a liquid jet looks almost like a cylinder with a spherical nose. Nevertheless, as a common phenomenon, a vortex could occur just beneath the impact point of either a drop or the tip of a micro-jet. If a satellite drop impacts on the cavity bottom with either a mistimed arrival or an insufficient amount of impact energy, the bubble separation never occurs, leaving only a small and shallow depression on the surface which will change into a water jet without containing air bubbles. Contrary to this, when an air bubble is formed as a result of a small volume of air cavity separation, two fine re-entrant jets are produced at the separation point and driven due to capillary pressures in opposite directions. For a short period after the bubble formation, an air bubble oscillates while moving slightly downward away from the water surface. As seen in figure 5, this phenomenon progresses with time while the free surface maintains its upward motion based on the conservation of momentum of the water. Consequently the bubble stops its downward motion. A water jet is formed at the central part of the free surface, developing into a water column. This phenomenon occurs whether air bubble is created or not.

3.2. *Characteristics of a water column developed from a splash jet*

The location of an entrapped air bubble inside a water column depends on the timing of air bubble formation, in other words the period of satellite drop impact. A water column reaches its maximum height, $h_{c,max}$, and thereafter falls vertically. The maximum column height, $h_{c,max}/d_D$, is plotted in figure 11(*a*) against *We* for three drop diameters, i.e. $d_D = 5.2$, 5.7 and 6.2 mm. Solid symbols are the cases where no drop separation occurs and open symbols correspond to the drop separation during the falling process. In the range of $We \leqslant 300$ (corresponding to $Fr \leqslant 60$), which is the

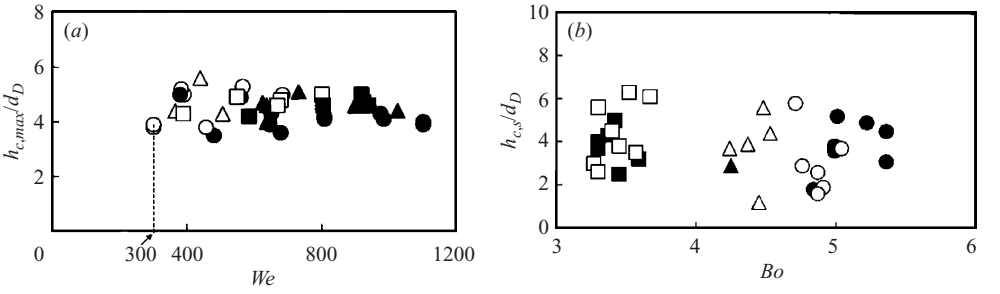

FIGURE 11. (*a*) Maximum water column height $h_{c,max}$ as a function of *We* and (*b*) the column height at separation $h_{c,s}$ as a function of *Bo* for three drop diameters $d_D = 6.2$ (○, ●), 5.7 (△, ▲) and 5.2 (□, ■) mm; both heights are divided by the primary drop diameter d_D.

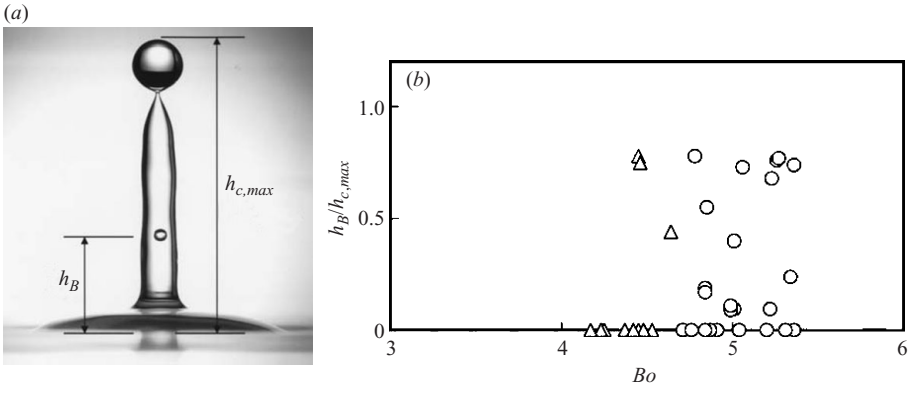

FIGURE 12. Water column formation and air bubble entrainment: (*a*) an image near the maximum height of a water column, which contains an air bubble. This picture was taken with the exposure time of 2 μs for the conditions of $d_D = 6.2$ mm, $Fr = 92$ and $We = 472$. (*b*) Air bubble location, h_B, at the maximum water column height divided by $h_{c,max}$ as a function of *Bo*.

region to the left of the dashed line on figure 11(*a*), a rising water column separated to create a drop before attaining its maximum height. Consequently there were no data for $h_{c,max}/d_D$ in this region. For the region $We > 300$ ($Fr > 60$), it is apparent that $h_{c,max}/d_D$ is almost constant with an average value of 4.4, but fluctuating between 3.5 and 5.6. These values are larger than those measured by Liow (2001), i.e. 2.85–4.17, which were for a small drop of 2.1 mm in diameter for the range $454 < Fr < 711$. In the larger *We* region, $We > 800$, a water column does not cause separation. This is a completely different feature from the range $We < 800$ where drop separation occurs in the falling process.

Figure 11(*b*) shows the drop separation position from a water column, $h_{c,s}$, as a function of the Bond number, which involves two possible separations. One arises during the rising process where the $h_{c,s}$ is shown by solid symbols, and another occurs during the falling process after the point of $h_{c,max}$ as shown by open symbols. In this case *Bo* was calculated by employing the individual diameters of each drops, without adopting any averaging. It is seen that $h_{c,s}/d_D$ roughly decreases with increasing *Bo* although the dispersion of the results is relatively large. In contrast to the behaviour of $h_{c,max}$, we notice an wider drop separation for a narrower change in *Bo*, because breakup phenomena are sensitive to a disturbance induced during the water column motion. Figure 12 shows (*a*) a snapshot of a water column at maximum height, $h_{c,max}$,

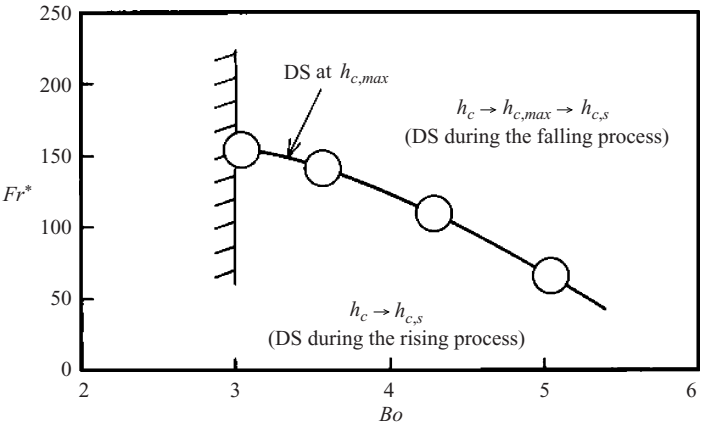

FIGURE 13. Critical Froude number, $Fr*$, for the criterion of drop separation, where a drop is detached from the top of a water column at the maximum height, as a function of the Bond number. Below the curve drop separation occurs during the rising process and above it during the falling process. DS means the point of drop separation.

and (*b*) the dimensionless air bubble location, $h_B/h_{c,max}$, as a function of Bo for the case of $d_D = 6.2$ mm ($Fr = 92$, $We = 472$). The angle subtended by the water column just below the separating point prior to detachment was found as 43°, whereas Liow (2001) reported angles between 31° and 34° for spherical drops with diameter of around 2.1 mm.

Figure 12(*b*) shows the Bo range where an air bubble can exist inside a water column. Air bubble entrapment occurs probabilistically in the range $4.4 < Bo < 5.4$ and $Fr < 150$ when the drop diameters are 5.7 and 6.2 mm, but no air bubble appears for the drop diameters less than 5.2 mm. The maximum height of an air bubble drawn up inside a water column, $h_B/h_{c,max}$, is around 0.8. For convenience no entrained air bubbles are plotted on the zero line, i.e. $h_B/h_{c,max} = 0$, in the figure. Thus water column motion can be characterized by two significant factors: the air bubble itself and whether drop separation occurs or not. As easily imagined from figure 12(*a*), when a drop is detached from the top of a water column a bifurcation of air flow could be induced around the necking point (Peregrine *et al.* 1990). Afterwards capillary waves are generated and travel over the column surface (see figures 14 and 15*a*). As is well-known the propagation velocity of a capillary wave, V_c, can be expressed as

$$V_c = \sqrt{\frac{2\pi\sigma}{\rho\lambda}}, \tag{4}$$

where λ is the wavelength of a capillary wave (Rayleigh 1894; Liow 2001). Figure 13 shows the critical Fr, Fr^*, against Bo with DS denoting the drop separation during its motion. The condition of Fr^* implies the situation where a drop is detached from the top of a water column just at its maximum height. In the region below the Fr^* curve, drop separation occurs during the rising process, which can be expressed as $h_c \rightarrow h_{c,s}$. On the other hand, in the region above the Fr^* curve, drop separation takes place during the falling process, expressed as $h_c \rightarrow h_{c,max} \rightarrow h_{c,s}$.

There is another possibility of the presence of air bubbles entrapped in a water column. Franz (1959) observed minute bubbles within a water column during a period where an isolated air bubble due to satellite impact still remained in the water beneath

FIGURE 14. An oblique view of a falling water column for the initial conditions of $d_D = 6.2$ mm, $Fr = 130$ and $We = 663$ ($Bo = 5.2$). Drop separation occurs and air bubbles are observable at the bottom of the drop. The column base is not deep but free surface swelling can be clearly seen.

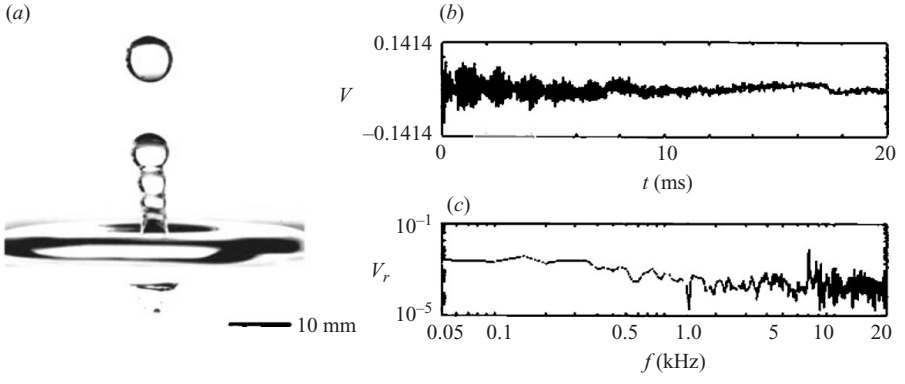

FIGURE 15. (a) Surface breakup due to the collapse of a water column falling without air bubbles, for $d_D = 5.7$ mm, $Fr = 142$ and $We = 619$ ($Bo = 4.4$); $t = 160$ ms. The corresponding underwater sound signal is indicated in (b) as a time sequence and (c) is its power spectrum.

the free surface (see figure 3 in his paper). This could result from another impact of small drops split from the edge of a re-entrant jet produced after the satellite impact, which emerged from the water layer into the air. Figure 14 is a single shot of a falling water column taken from a slightly oblique direction above the free surface, indicating drop separation at the top and the free surface swelling. An air bubble can be clearly seen at the bottom of the drop. Figure 14 looks very similar to the image shown in figure 15(a). Although both figures 14 and 15(a) correspond to the case where drop separation occurs during the falling of a water column, as conjectured from figure 13, no air bubble is contained within the separated drop in figure 15(a).

3.3. *Surface breakup and the second bubble formation*

Figure 15(a) is an example of surface breakup for the case of $Fr = 142$ ($d_D = 5.7$ mm) and $t = 160$ ms, together simultaneously recorded (b) underwater sound and (c) its power spectrum. In this case, a drop 7.4 mm in diameter, obviously larger than the

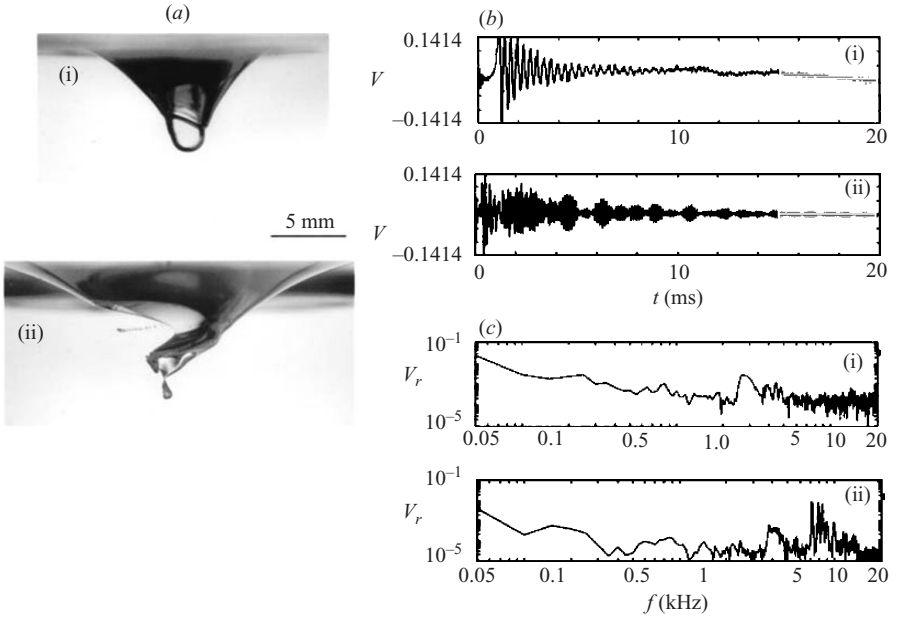

FIGURE 16. Surface contact and partial breakup near the bottom of a curved water surface for (*a*)(i) $d_D = 6.2$ mm, $Fr = 227$, $We = 1137$ and (*a*)(ii) $d_D = 6.2$ mm, $Fr = 140$, $We = 722$. Snapshots were taken at (*a*)(i) $t = 171$ ms and (*a*)(ii) $t = 183$ ms. The induced underwater sound signals are shown in (*b*)(i) and (*b*)(ii) and their power spectra in (*c*)(i) and (*c*)(ii), respectively.

impacting drop size ($d_D = 5.7$ mm), was detached from a water column during its falling process and no air bubbles were observed inside the water column. Capillary waves are clearly visible and surface breakup is generated somewhere underneath the free surface. Consequently underwater sound with higher frequencies was generated as recorded in figure 15(*b*) and analysed in 15(*c*). Near the column base the fluctuating surface approaches the curved free surface with a large curvature, inducing a circular air flow between the two water–air interfaces. A Rayleigh–Taylor instability may be amplified during this process due to the increase in acceleration of the interface in the normal direction. Therefore, when one of the crests on the fluctuating column surface meets part of the curved water surface, the gap between the two surfaces decreases, eventually approaching a critical value of order of about 0.01 μm below which the van der Waals attraction force is dominant (Duineveld 1998). Consequently film rupture occurs as a result of the contact of the two interfaces, resulting in the formation of a cusp which moves away from the point of contact. The cusp is driven by the capillary pressure to evolve smoothly. This is suggested as a scheme of the process of surface breakup (Shikhmurzaev 2001). Since the breakup phenomenon is unstable, air masses of various size will individually disintegrate into much smaller bubbles. A transient oscillation of these bubbles can cause underwater sounds, called the second bubble sound, which corresponds to C in figure 5.

Figure 16 shows two other examples of surface breakup phenomena for the cases where (*a*)(i) $d_D = 6.2$ mm, $Fr = 221$, $We = 1137$ and (*a*)(ii) $d_D = 6.2$ mm, $Fr = 140$, $We = 722$. Two photographs were taken at $t = 171$ ms for the former and at $t = 183$ ms for the latter, showing the surface contact and subsequent breakup phenomena. In figure 16(*a*)(i) capillary waves are clearly observed, propagating away from the contact point with the velocity of $1.3\ \mathrm{m\,s^{-1}}$ which can be determined using equation (4) since

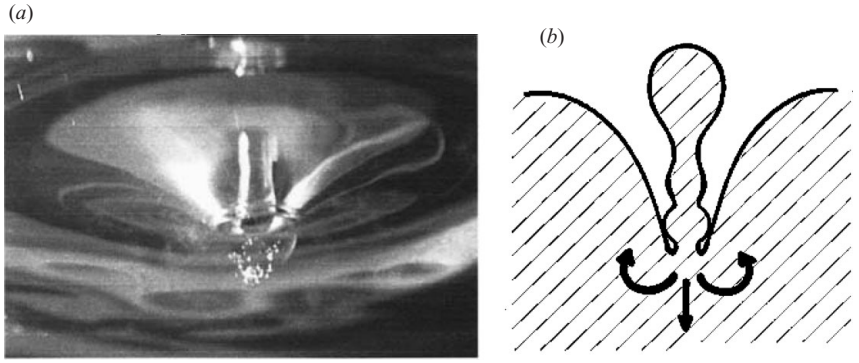

FIGURE 17. Surface breakup due to the contact of the curved free surface with the fluctuating water column surface without air bubbles for the case of $d_D = 6.2$ mm, $Fr = 130$ and $We = 663$: (*a*) a snapshot taken from a slightly oblique direction in water at $t = 168$ ms; (*b*) a sketch of the surface contact.

the wavelength of the capillary wave, λ, was measured to be 0.28 mm. The transient underwater sound indicates a damped oscillation with a prominent frequency of about 2.5 kHz starting at 1 ms after this snapshot, which corresponds to the elapse time of 172 ms after the impact. Applying equation (3) to estimate the equivalent radius of a spherical bubble gives 1.3 mm. The correlation between the breakup time and the onset time of underwater sounds was confirmed with quite excellent agreement. When no drop separation occurred, surface breakup tended to take place relatively deeper in the water.

The case shown in figure 16(*a*)(ii) indicates a partial breakup due to the non-axial symmetric contact between the water column surface and the curved free surface, at the bottom of which an air bubble with 0.40 mm radius is on the point of creation. Using (3), we can evaluate the resonant frequency to be 8.2 kHz, which is very close to one of the peak frequencies in the power spectrum in figure 16(*c*)(ii).

Figure 17 shows another example of surface breakup taken at $t = 168$ ms for the condition of $d_D = 6.2$ mm ($Fr = 130$, $We = 663$). The photograph was captured in a slightly oblique direction underneath the free surface, enabling us to see a three-dimensional view of a water column although the image was refracted. In this case a pure water column, implying no air bubbles inside, is falling without drop separation. A bubble cluster, consisting of numerous small bubbles, is formed as a result of the contact between the water column surface and the curved free surface. A sketch of the surface contact is given in figure 17(*b*). On the other hand, when an air bubble is trapped inside a water column, it moves along with the column as demonstrated in figure 5.

Figure 18 shows two snapshots of the phenomena near the water column base for $d_D = 6.2$ mm ($Fr = 130$, $We = 663$). They were taken at (*a*) $t = 179$ ms, indicating an instant before the surface breakup, and at (*b*) $t = 185$ ms, after the breakup. Observations showed that the surface breakup position, h_r, closely related to the location of an air bubble as typically shown in figure 18(*b*). Figure 19 is a close-up double exposure photograph taken with the time difference of 1 ms for the same conditions as figure 18. An air bubble is clearly observed and its location is very near to the surface breakup position. It was found that the breakup position was less related to whether the column motion was growing or falling, although the surface

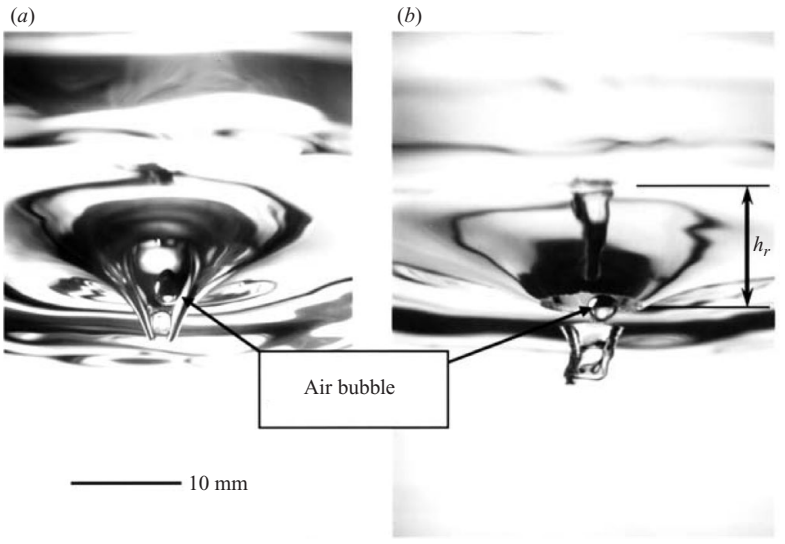

FIGURE 18. Two stages of an oblique view of the base of a falling water column which connects to a highly curved free surface. The photographs were taken at (*a*) 179 ms (before breakup) and (*b*) 185 ms (immediately after the breakup) for the case of $d_D = 6.2$ mm, $Fr = 130$ and $We = 663$. An air bubble is seen inside each water column.

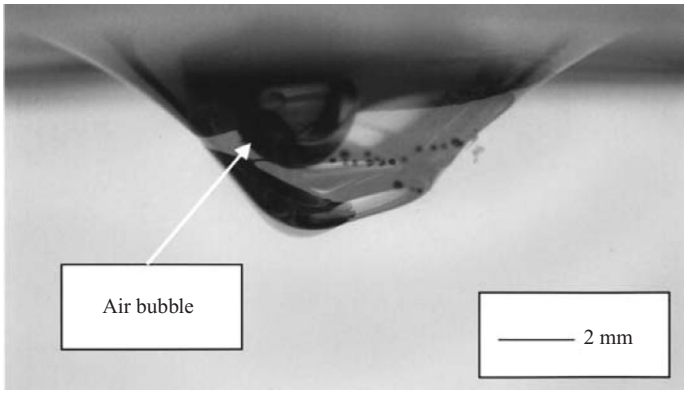

FIGURE 19. Double exposure photograph for the conditions of $d_D = 6.2$ mm, $Fr = 130$ and $We = 663$. The first image was taken at $t = 171$ ms and 1 ms later the other Xenon flash was illuminated for capturing the second image. During this time difference surface breakup occurred.

contact itself was affected by whether drop detachment occurred from a water column or not.

The dimensionless breakup position, h_r/d_D, is now examined by changing Fr and drop aspect ratio, χ, and the results are illustrated in figure 20(a, b). Note that in figure 20(a) the data points on the zero line imply the situation where no surface breakup occurred. Solid symbols are the data for a water column containing an air bubble, which are available in the range $Fr < 150$. It is also found that the deepest breakup is achieved when Fr is between 110 and 140. For $Fr < 50$, however, the breakup associated with the surface contact never occurred, resulting in no second bubble sound. For larger Froude numbers the breakup position is likely to be between 0.5 and 0.9. In the

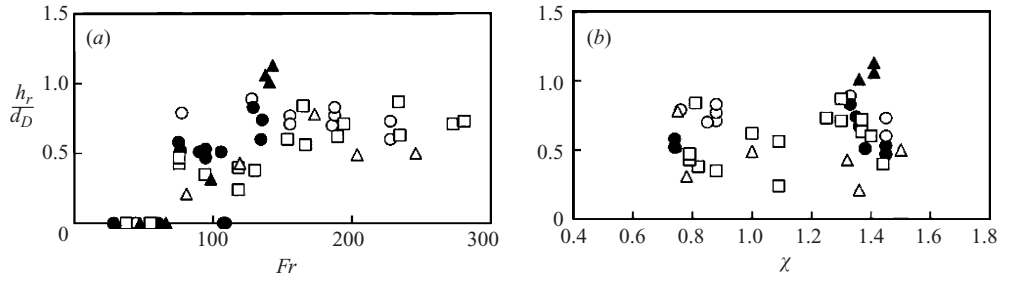

FIGURE 20. Surface breakup positions as a function of (*a*) the Froude number, *Fr*, and (*b*) the primary drop aspect ratio χ at impact, where drop diameter d_D : 6.2 mm (○, ●), 5.7 mm (△, ▲) and 5.2 mm (□, ■). ○, △, □: without air bubble; ●, ▲, ■: with air bubble.

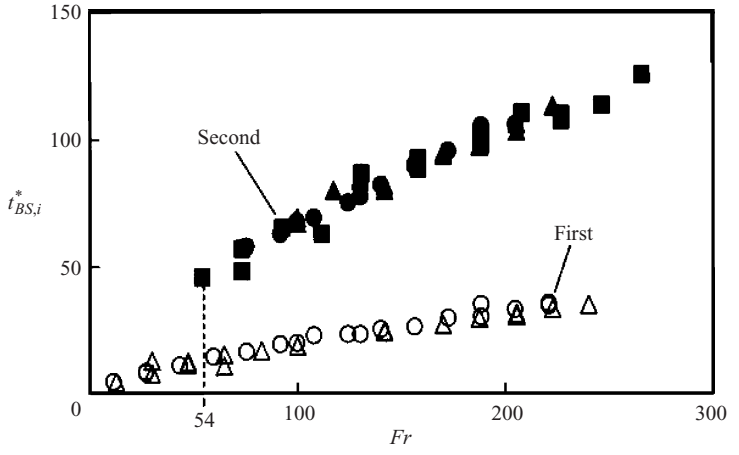

FIGURE 21. Froude number dependence of the onset times of the first and second bubble sounds for three diameters $d_D = 6.2$ mm (○, ●), 5.7 mm(△, ▲) and 5.2 mm (□, ■), where ○, △, □: first bubble sounds; ●, ▲, ■: second bubble sounds.

present experiment, there exists a critical Bond number below which a water column never contains air bubbles as a source of the first underwater sound, estimated to be $Bo = 4.5$. The surface breakup position is also examined for the drop aspect ratio χ as shown in figure 20(*b*). From the data dispersion we see that there may exist two groups. One group is at around $\chi \sim 1.4$ and the other at $\chi < 1.1$, where $\chi < 1$ implies a slender drop whose impact is followed by weak splashes, whereas $\chi > 1$ being an oblate drop results in many vivid splashes. Obviously the latter case, $\chi > 1$, has a wide range of h_r/d_D. Presumably, the extent of surface breakup is connected to the behaviour of splashes. The surface contact at the deepest position occurs when χ is about 1.4.

3.4. *Bubble sounds and their application to an open-type Suikinkutsu*

The present experiment shows that the first bubble sound is initiated at $Fr = 10$, i.e. corresponding to $H_N = 50$ mm, and its onset time is around 50 ms measured from the drop impact, although its occurrence probability is rather low, about 20 %. The second bubble sound also involves probability. Taking d_D/V_{imp} as the characteristic time, we can define the dimensionless onset time as $t^*_{BS,i} = t_{BS,i}/(d_D/V_{imp})$ with $t_{BS,i}$ being the onset time of the ith bubble sound ($i = 1,2$). Figure 21 shows the experimental data of

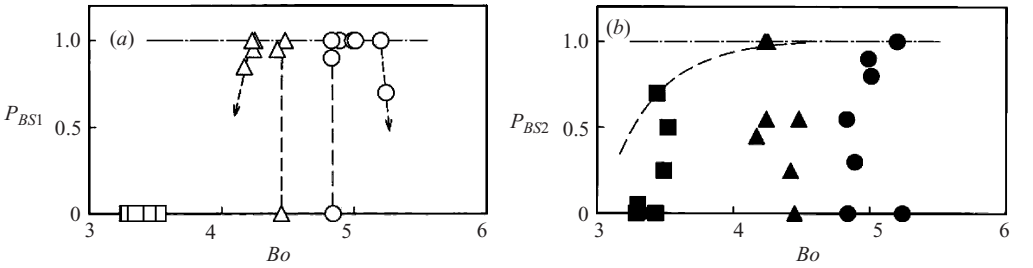

FIGURE 22. Bond number dependence of the occurrence probabilities for (*a*) the first bubble sounds (○, △, □) and (*b*) second bubble sounds (●, ▲, ■), where $d_D = 6.2$ mm (○, ●), 5.7 mm (△, ▲) and 5.2 mm (□, ■).

$t^*_{BS,i}$ plotted against Fr. The second bubble sound starts at $Fr = 54$. Each dimensionless onset time of the bubble sounds increases as Fr increases. By taking twenty data points for each dripping height H_N the probability of occurrence of bubble sounds has been examined by changing Bo.

Figure 22 shows two cases, indicating (*a*) the first bubble sound and (*b*) the second bubble sound. It is found for the first bubble sound that there are some regions where almost 100 % sound generation probabilty is achieved for the drop diameters of 5.7 and 6.2 mm, but 0 % for the 5.2 mm sized drop. For the second bubble sound generation, on the other hand, the probabilities scatter between zero to 100 % for each average drop diameter.

A special difference from the first bubble sound is shown in figure 22(*b*), where second bubble sounds due to the 5.2 mm drop impact exist, although its maximum probability is 70 %. In the present experiment the first bubble sounds range from 1 kHz to 7 kHz, for $10 < Fr < 240$, whereas the second bubble sounds are further scattered from about 1 kHz to 13 kHz for $50 < Fr < 280$. It should be mentioned that there is a third underwater sound, denoted by D in figure 5. This is due to the oscillation of air bubbles generated when the whole of a drop detached from a water column is touching the curved free surface. However the induced pressure fluctuation is very weak, so that no sound results.

The time difference between the sound signals B and C in figure 5(*c*) is 122 ms, which is longer than the audible time difference for human beings, i.e. 30–40 ms. Consequently we can hear the sequential sound as two separated sounds like 'Po—cha-n', which is an onomatopoeic sound in Japanese. 'Po' is due to the first bubble sound and 'cha-n' is due to the second bubble sound. When there is only one sound source, either the first or second bubble sound, we can hear a sound like 'Pocha'. These sounds are generated in an open water tank, allowing us to hear a drop less than 6.5 mm in diameter. On the other hand, if drop impact is generated inside a water jar, as in a Suikinkutsu, the sounds propagate through the water surface into the air inside the jar and reflect many times on its wall, producing a reverberant sound with a long duration which is peaceful and healing. It was found that when using a primary drop of 6.2 mm diameter the Suikinkutsu (see figure 2*b*) sounded like 'pi–yohnn' or 'co—hnn', which is a very clear sound with high-frequency components, similar to the sound generated by a 'harp'. This is why 'Suikinkutsu' is called 'water-harp-jar'.

As the primary drop size increases, the volume of entrained air also increases and we obtain underwater sounds with a wide range of frequencies: the bigger the drop, the more powerful the sounds.

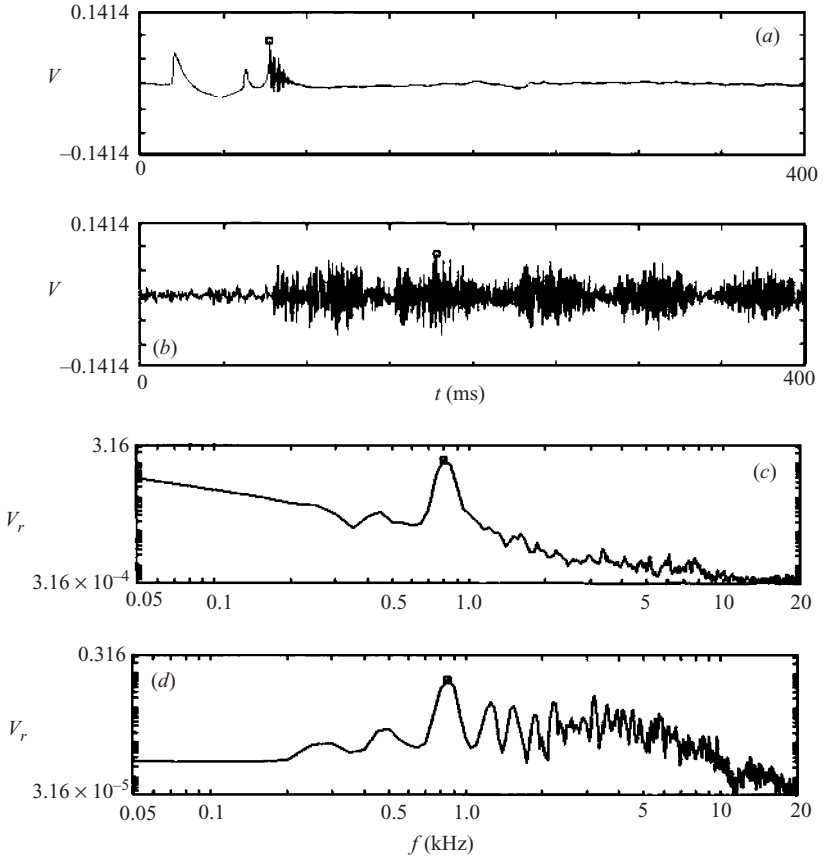

FIGURE 23. Underwater sound and Suikinkutsu sound measurement: (*a*) an underwater sound signal from the 7.2 mm sized drop impact and (*b*) the corresponding Suikinkutsu sound signal. (*c*) and (*d*) The average power spectra of underwater sounds and Suikinkutsu sounds, measured by taking twenty data points for the same conditions where the drop diameter was 7.8 mm, the dripping height was 500 mm and the water temperature was kept constant at 2 °C.

Figure 23 shows four examples of sound signals together with power spectra. Figures 23(*a*) and 23(*b*) are the measured sound signals for the case of a drop with 7.2 mm diameter, showing an underwater sound pressure trace and an open-type Suikinkutsu sound pressure signal, respectively, where the recording time is 400 ms. Figures 23(*c*) and 23(*d*) are two average power spectra taken with twenty data points for each recording time of 20 ms, showing an average underwater sound and an average Suikinkutsu sound, respectively, where the average drop diameter was 7.8 mm, the dripping height 500 mm and the water temperature was kept constant at 2 °C. The underwater sound, figure 23(*a*), contains two pressure fluctuations due to the primary and satellite drop impacts, followed by the damped oscillation with high frequencies resulting from the first bubble oscillation; there is no signal due to the second bubble sound. This is a special feature of primary drops larger than 7.0 mm in diameter, confirmed from the high-speed video photography where no bubble formation resulted during the collapse of a water column, causing no second bubble sound. On the other hand, the Suikinkutsu sound, figure 23(*b*), was found to last for a long time as a result of multiple reflections of the first bubble sound on the inner surface of the jar, creating a reverberant sound with a duration of 0.7–1.0 s. Actual

Suikinkutsu sound is longer than this, by roughly 30 %, because of the resonant effect of a water jar. Naturally it is important to control the quantity of water flowing downwards to impact onto a free surface. Watanabe (2004) recommended a drop period of 2 s. Our Suikinkutsu suggested that an optimum water rate was 0.25 ml s^{-1}, which corresponded to a primary drop with diameter 8.0 mm, and the Suikinkutsu sound measured outside the water jar lasted for 1.7 s, which is close to the Watanabe's optimum drop period.

Regarding figures 23(*c*) and 23(*d*), the average underwater sound spectrum exhibits a prominent peak at around 0.8 kHz, which corresponds to the damped oscillation of an equivalent bubble radius of 4.1 mm as confirmed from the high-speed photography. Since an underwater sound wave passes through the water surface to the air and reflects on the inner surface of the jar many times to cause a resonant sound, Suikinkutsu sound tends to contain a wide range of frequency components as the fundamental tone is very near the first bubble sound, including harmonic sound. As indicated in figure 23(*d*) the Suikinkutsu sound has a peak power at the frequency of 0.85 kHz, which is exactly coincident with the frequency of Hana Suikinkutsu (Watanabe 2004). Our Suikinkutsu sounded like 'Go—hnn' which is very similar to that generated by a Japanese temple bell.

In addition we explored the water temperature effect, in terms of the surface tension effect, on the Suikinkutsu sound as it is a significant factor in underwater sound generation. Using the setup described in figure 2(*b*) we measured the Suikinkutsu sound for three different water temperatures, 2 °C, 20 °C and 40 °C, where the drop diameter was 7.8 mm and the dripping height 500 mm. It was found that the Suikinkutsu sound decreases in power as the water temperature increases, or in other words, the surface tension decreases. To generate a powerful sound of the Suikinkutsu, therefore, water temperature should be maintained as low as possible.

4. Conclusions

Underwater sounds due to bubble oscillation generated by drop impact in the irregular entrainment region have been experimentally investigated for drops mainly with diameters 5.2, 5.7 and 6.2 mm, all of which were accompanied by single satellite drops. Surface breakup is a key phenomenon in creating either a single air bubble or multiple bubbles. A series of underwater sounds was generated even for the single drop impact case, and among those two audible sounds are prominent. The first sound originated from the oscillation of an air bubble produced by the separation of an elongated cavity behind a satellite drop which occurred at the bottom of a curved free surface under contraction. On the other hand, the second underwater sound was caused by the oscillation of air bubbles generated during the collapse of a water column. Sometimes, however, an underwater sound was occupied by only one sound source of either the first bubble sound or the second one. The dimensionless onset times of the first and second bubble sounds depended on the Froude number and their occurrence probabilities were widely spread. In addition the presence of an air bubble, trapped in a water column, was considered to be an important factor enhancing the surface contact probability between the column surface and curved free surface. It was verified that our Suikinkutsu could generate very clear sounds, especially when the water temperature was maintained low

The authors would like to express their thanks to the referees for their fruitful suggestions and comments. They are grateful to Mr Y. Hamada of SANPICO Ltd. for his skillful technique in high-speed photography. They also thank Mr M. J. Crawford

for his assistance with the manuscript. Assistance in conducting some of the present experiment was received from the first author's students, Mr T. Kasai, S. Miura and C. Yamada, with acknowledgements. This study was supported by a grant from the Japan Society for the Promotion of Science for the Grant-in-Aid for Scientific Research (C) in 2005–2006.

REFERENCES

Blake, J. R., Tomita, Y. & Tong, R. P. 1998 The art, craft and science of modeling jet impact in a collapsing cavitation bubble. *Appl. Sci. Res.* **58**, 77–90.

Bourne, N. K., Obara, T. & Field, J. E. 1996 The impact and penetration of a water surface by a liquid jet. *Proc. R. Soc. Lond.* A **452**, 1497–1502.

Chapman, D. S. & Critchlow, P. R. 1967 Formation of vortex rings from falling drops. *J. Fluid Mech.* **29**, 177–185.

Duineveld, P. C. 1998 Bouncing and coalescence of bubble pairs rising at high Reynolds number in pure water or aqueous surfactant solutions. *Appl. Sci. Res.* **58**, 409–439.

Franz, G. J. 1959 Splashes as sources of sound in liquids. *J. Acoust. Soc. Am.* **31**, 1080–1096.

Liow, J.-L. 2001 Splash formation by spherical drops. *J. Fluid Mech.* **427**, 73–105.

Medwin, H., Kurgan, A. & Nystuen, J. A. 1990 Impact and bubble sound from raindrops at normal and oblique incidence. *J. Acoust. Soc. Am.* **88**, 413–418.

Minnaert, M. 1933 On musical air-bubbles and the sounds of running water. *Phi. Mag.* **16**, 235–248.

Nystuen, J. A. 1986 Rainfall measurements using underwater ambient noise. *J. Acoust. Soc. Am.* **79**, 972–982.

Obara, T., Bourne, N. K. & Field, J. E. 1995 Liquid-jet impact on liquid and solid surfaces. *Wear* **186–187**, 388–394.

Oguz, H. N. & Prosperetti, A. 1990 Bubble entrainment by the impact of drops on liquid surfaces. *J. Fluid Mech.* **219**, 143–179.

Peregrine, D. H., Shoker, G. & Symon, A. 1990 The bifurcation of liquid bridges. *J. Fluid Mech.* **212**, 25–39.

Prosperetti, A., Crum, L. A. & Pumphrey, H. C. 1989 The underwater noise of rain. *J. Geophys. Res.* **94**, 3255–3259.

Prosperetti, A. & Oguz, H. N. 1993 The impact of drops on liquid surfaces and the underwater noise of rain. *Annu. Rev. Fluid Mech.* **25**, 577–602.

Pumphrey, H. C. & Elmore, P. A. 1990 The entrainment of bubbles by drop impacts. *J. Fluid Mech.* **220**, 539–567.

Rayleigh, Lord 1894 *Theory of Sound*, 2nd Edn. Macmillan. (Reprinted 1945, Dover Press.)

Scrimger, J. A. 1985 Underwater noise caused by precipitation. *Nature* **318**, 647–649.

Shikhmurzaev, Y. D. 2001 Coalescence and breakup: solutions without singularities. *IUTAM Symp. on Free Surface Flows* (ed. A. C. King & Y. D. Shikhmurzaev), pp. 281–288. Kluwer.

Strasberg, M. 1956 Gas bubbles as sources of sound in liquids. *J. Acoust. Soc. Am.* **28**, 20–26.

Tatsui, T. 2000 *A Story of Suikinkutsu.* Kenchiku Shiryo Kenkyuusya Co. Ltd. (in Japanese).

Thoroddsen, S. T., Etoh, T. G. & Takehara, K. 2003 Air entrapment under an impacting drop. *J. Fluid Mech.* **478**, 125–134.

Tomita, Y. 2004 Suikinkutsu, water-harp-jar. In *Encyclopedia of Flow Phenomena* (ed. T. Kambe), pp. 294–295. Maruzen (in Japanese).

Tomita, Y., Kasai, T. & Miura, S. 2003 Irregular bubble entrainment following drop impact on a free surface. *Proc. 2003 ASME Cavitation and Multiphase Forum, Honolulu, Hawaii, USA* (ed. C. E. Brennen), FEDSM2003–45015.

Tomita, Y. & Shima, A. 1990 High-speed photographic observations of laser-induced cavitation bubbles in water. *Acustica* **71**, 161–171.

Watanabe, Y. 2004 Analytical study of acoustic mechanism of 'Suikinkutsu'. *Japan. J. Appl. Phys.* **43**, **9A**, 6429–6443.

Worthington, A. M. 1908 *A Study of Splashes.* Longmans, Green and Co.

Zhang, X. & Basaran, O. A. 1995 An experimental study of dynamics of drop formation. *Phys. Fluids* **7**, 1184–1203.